Inferring fault rheology from low-frequency earthquakes on the San Andreas

N. M. Beeler,[1] Amanda Thomas,[2] Roland Bürgmann,[2] and David Shelly[3]

Received 12 February 2013; revised 21 October 2013; accepted 24 October 2013; published 27 November 2013.

[1] Families of recurring low-frequency earthquakes (LFEs) within nonvolcanic tremor (NVT) on the San Andreas fault in central California show strong sensitivity to shear stress induced by the daily tidal cycle. LFEs occur at all levels of the tidal shear stress and are in phase with the very small, ~400 Pa, stress amplitude. To quantitatively explain the correlation, we use a model from the existing literature that assumes the LFE sources are small, persistent regions that repeatedly fail during shear of a much larger scale, otherwise aseismically creeping fault zone. The LFE source patches see tectonic loading, creep of the surrounding fault which may be modulated by the tidal stress, and direct tidal loading. If the patches are small relative to the surrounding creeping fault then the stressing is dominated by fault creep, and if patch failure occurs at a threshold stress, then the resulting seismicity rate is proportional to the fault creep rate or fault zone strain rate. Using the seismicity rate as a proxy for strain rate and the tidal shear stress, we fit the data with possible fault rheologies that produce creep in laboratory experiments at temperatures of 400 to 600°C appropriate for the LFE source depth. The rheological properties of rock-forming minerals for dislocation creep and dislocation glide are not consistent with the observed fault creep because strong correlation between small stress perturbations and strain rate requires perturbation on the order of the ambient stress. The observed tidal modulation restricts ambient stress to be at most a few kilopascal, much lower than rock strength. A purely rate dependent friction is consistent with the observations only if the product of the friction rate dependence and effective normal stress is ~ 0.5 kPa. Extrapolating the friction rate strengthening dependence of phyllosilicates (talc) to depth would require the effective normal stress to be ~50 kPa, implying pore pressure is lithostatic. If the LFE source is on the order of tens of meters, as required by the model, rate-weakening friction rate dependence (e.g., olivine) at 400 to 600°C requires that the minimum effective pressure at the LFE source is ~ 2.5 MPa.

Citation: Beeler, N. M., A. Thomas, R. Bürgmann, and D. Shelly (2013), Inferring fault rheology from low-frequency earthquakes on the San Andreas, *J. Geophys. Res. Solid Earth, 118*, 5976–5990, doi:10.1002/2013JB010118.

1. Introduction—Nonvolcanic Tremor

[2] Deep slip in some subduction zones is accompanied by long duration seismic signals with highest signal-to-noise ratios in the ~2–8 Hz band, of similar frequency to volcanic tremor. Because it is associated with plate boundary faults, this seismicity is often referred to as tectonic tremor or generally as nonvolcanic tremor (NVT) [*Obara*, 2002]. The seismic moment of the tremor is a tiny fraction of the total moment of the deep slip [*Kao et al*., 2010]. In Japan and elsewhere, some of the tremor is located very near the inferred position of the subduction megathrust fault that is assumed to be the locus of slip. *Shelly et al*. [2007a] argued that at least part of the tremor signal is generated by slip on small on-fault asperities and showed that individual repeating low-frequency earthquakes (LFEs) make up a portion of the tremor. Focal mechanism inversions of LFEs in Shikoku Japan indicate that they are generated by shear slip in an orientation consistent with the plate boundary [*Ide et al*., 2007b]. Other studies elsewhere have reported intraplate NVT locations [e.g., *Kao et al*., 2005], and tremor location relative to the presumed fault plane remains somewhat controversial. Nevertheless, a simple, popular conceptual model for LFEs is that they represent radiation emanating from small, persistent regions that repeatedly fail during aseismic shear of the larger-scale surrounding fault zone [*Shelly et al*., 2007a]. In the present paper, we implement a quantitative version of this model to study the sensitivity of NVT to impose changes in stress.

[3] Nonvolcanic tremor [*Nadeau and Guilhem*, 2009] and LFEs extracted from the tremor [*Shelly and Hardebeck*, 2010] also occur on the deep San Andreas fault (SAF). It is these LFEs that are the topic of the present paper, and we use aspects

[1]Cascades Observatory, U.S. Geological Survey, Vancouver, Washington, USA.
[2]University of California, Berkeley, California, USA.
[3]U.S. Geological Survey, Menlo Park, California, USA.

Corresponding author: N. M. Beeler, Cascades Observatory, U.S. Geological Survey, 1300 Cardinal Court, Bldg. 10, Suite 100, Vancouver, WA 98683, USA. (nbeeler@usgs.gov)

2169-9313/13/10.1002/2013JB010118

This article was corrected on 7 MAY 2014. See the end of the full text for details.

of their occurrence and rate of occurrence to constrain the rheology that controls aseismic fault slip in the source region. The LFEs locate between 16 and 29 km depth. Unlike in subduction zones, NVT and associated LFEs on the San Andreas are not associated with geodetically detectable episodes of transient rapid fault creep [*Smith and Gomberg*, 2009]. However, tremor on the SAF is episodic at shorter recurrence intervals and is distributed over smaller regions than in subduction zones. Typical episodic recurrence of SAF tremor ranges from 1 to greater than 4 months [*Guilhem and Nadeau*, 2012], compared with 6–15 months for geodetically detectible slip in subduction zones. Furthermore, NVT/LFE rates show other evidence of being associated with deep slip such as spatiotemporal propagation [*Shelly*, 2009] and accelerated occurrence rates associated with the 2004 Parkfield earthquake [*Shelly and Johnson*, 2011]. Thus, despite a lack of geodetically detectable transient slip, NVT and LFEs on the SAF are thought to be the seismic manifestation of deep, largely aseismic slip in the region [*Shelly*, 2009].

[4] One characteristic common to observations of NVT and LFEs in subduction zones and on the SAF that distinguishes them from shallow seismicity is sensitivity to small stress perturbations. Studies of static stress changes from regional earthquakes report both an aftershock-like response of deep NVT and LFEs on the SAF to increases of 6 and 10 kPa in shear stress from the 2003 M_w 6.5 San Simeon and the 2004 M_w 6.0 Parkfield earthquakes, respectively, and quiescent response to decreases in stress [*Nadeau and Guilhem*, 2009; *Shelly and Johnson*, 2011]. Several studies report triggering of NVT and LFEs on the SAF and elsewhere by teleseismic surface and body waves that imposed stress transients as small as a few kilopascals [*Gomberg et al*., 2008; *Miyazawa and Brodsky*, 2008; *Peng et al*., 2009; *Hill*, 2010; *Ghosh et al*., 2009; *Shelly et al*., 2011]. Additionally, studies of tidal stress perturbations conclude that NVT and slow slip itself are sensitive to stress changes as small as fractions of a kilopascal [*Rubinstein et al*., 2008; *Nakata et al*., 2008; *Lambert et al*., 2009; *Thomas et al*., 2009; *Hawthorne and Rubin*, 2010].

1.1. Laboratory Models of Tidal Triggering

[5] Unlike NVT, many large, shallow earthquake catalogs have no little or no statistically significant relationship between earthquake occurrence and the solid earth tides [*Knopoff*, 1964; *Heaton*, 1982; *Vidale et al*., 1998; *Métivier et al*., 2009]. To explain this relation between the solid earth tides and earthquake occurrence, following *Dieterich* [1987], *Lockner and Beeler* [1999] conducted a series of laboratory friction experiments, extrapolated those to natural conditions, and argued that the tides and earthquakes are correlated but at a very low level, thus, providing an explanation why catalogs with very large event numbers are required to detect the correlation. The essential physical property of rock failure and friction that will prevent strong correlation between the tides and earthquakes is that the onset of rapid slip follows a long characteristic delay time. As a result, small amplitude stress changes with duration much shorter than the delay time have nearly no effect on the time of failure. This connection between delayed failure in rock mechanics tests and earthquake occurrence was first recognized by *Knopoff* [1964].

[6] The laboratory model [*Dieterich*, 1987; *Lockner and Beeler*, 1999; *Beeler and Lockner*, 2003] is for frictional failure due to elastic loading from tectonic stressing and the tides. Unlike the *Shelly et al*. [2007a] conceptual model for LFE occurrence, in the laboratory-based tidal triggering model there is no loading from fault creep. Mechanically, the model consists of a single degree of freedom frictional interface coupled to loading via an elastic element (slider-block). Accordingly, earthquake occurrence is sensitive to the tidal stresses as resolved into two specific stress components: the fault normal stress and the shear stress in the direction of fault slip. The model is assumed to apply to both the solid earth and the ocean tides. Ideally, correlations between the tides and earthquakes depend on fault orientation relative to the tidal stresses. In general for laboratory determined parameters, natural rates of tectonic stressing, hydrostatic pore fluid pressure, and tidal amplitudes in the range of kilopascal, this model predicts ~1% of earthquakes correlate with the tidal stress [*Lockner and Beeler*, 1999]. There are three specific predictions of this laboratory-based failure model that can be tested for earthquakes, including NVT and LFEs:

[7] For tidal loading resolved onto a fault as shear stress in the direction of slip and fault normal stress,

[8] 1. Events are expected to occur at all phases of the tides with the maximum rate of occurrence coincident with the maximum in the so-resolved tidal stress [*Dieterich*, 1987; *Lockner and Beeler*, 1999] and therefore can be thought of as "in phase" with the tidal stress.

[9] 2. The degree of correlation between the tidal stress and the rate of earthquake occurrence increases as the exponential of the ratio of the amplitude of the tidal stress to the ambient effective normal stress [*Dieterich*, 1987; *Beeler and Lockner*, 2003]. Thus, a correlation between the tidal stress and earthquake occurrence is much easier to detect if the tidal stress is high or the effective normal stress is low.

[10] 3. The characteristic delay time of failure is proportional to the effective normal stress and inversely proportional to the stressing rate [*Dieterich*, 1994; *Beeler and Lockner*, 2003].

[11] With regard to prediction (1), in a normal faulting environment, the Endeavor segment of the Juan de Fuca mid-ocean ridge, *Wilcock* [2001] found the maximum earthquake occurrence rate coincident with the maximum extensional ocean tidal stress. Similarly, *Cochran et al*. [2004] examined the relation between earthquake occurrence and phase of the ocean tidal stress and found the maximum rate of occurrence of shallow subduction thrust events coincided with the tidal maximum. NVT or LFEs in the Nankai and Cascadia subduction zones and on the SAF occur at all phases of the tides [*Nakata et al*., 2008; *Rubinstein et al*., 2008; *Thomas et al*., 2009]. Specifically, in Cascadia, *Lambert et al*. [2009] found tremor at all phases of the tidal stress and that the peak tremor activity coincides with maximum tidal shear stress resolved onto the subduction interface. Similarly, *Hawthorne and Rubin* [2010] found tremor rates enhanced at the time of the maximum shear stress in central Cascadia, and *Klaus et al*. [2011] report tremor amplitudes in phase with the tidal shear stress. Slow slip in Cascadia is also in phase with the NVT [*Hawthorne and Rubin*, 2010] but the relation to tidal stress is ambiguous due to uncertainty in the location of deep slip; their comparison between slip and the tides concludes that the phase of maximum strain rate in the daily tidal period may occur at the maximum shear stress or up to 90° before it.

[12] Similar modulation occurs in the Shikoku subduction zone of southwest Japan [*Shelly et al*., 2007b; *Nakata et al*.,

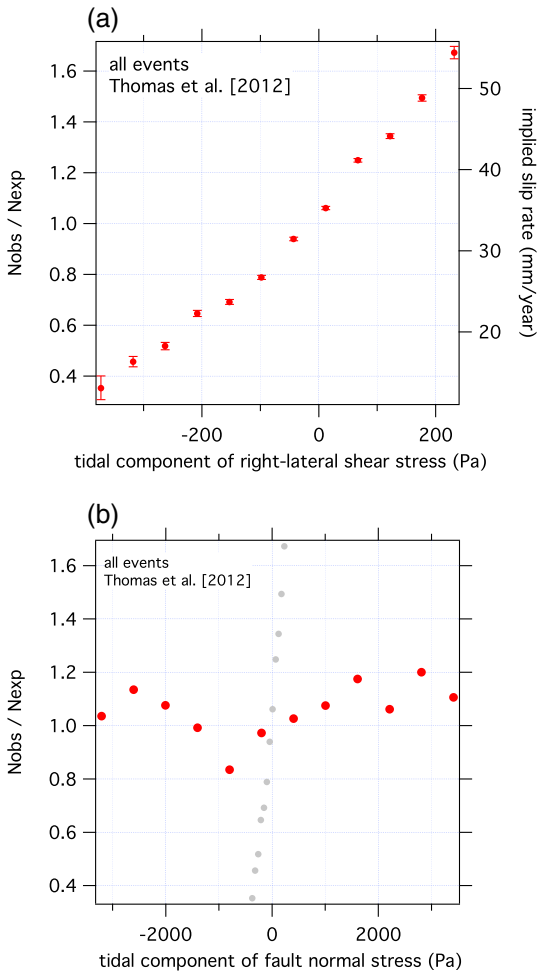

Figure 1. Relation between earthquake occurrence and the tidal shear stress from *Thomas et al*. [2012] for ~732,000 events in 88 LFE families. (a) The left vertical axis is the observed number of events normalized by the expected number. The error bars are the 99% bootstrap confidence intervals. The horizontal axis is the tidal shear stress. The right axis shows the implied slip rate provided equation 4c is appropriate and that the nominal creep rate is the plate motion rate, 31 mm/yr (see text). (b). Same as Figure 1a but for fault normal stress. Shown for reference are the shear stress data from Figure 1a (small grey symbols).

2008], and tremor occurs at all phases of the tides. *Nakata et al*. [2008] found that the tremor occurrence rate is well represented by a delayed failure model—they assumed that tidal loading at tremor sources is not amplified by fault creep and compared tremor with predictions using *Dieterich's* [1994] seismicity rate equations, given calculated theoretical tides in Shikoku. In both Nankai and Cascadia, high fluid pressures are inferred from V_p/V_s ratios in the NVT source region that have been invoked to explain correlation of NVT with small stress perturbations [*Shelly et al*., 2006; *Audet et al*., 2009]. On the San Andreas fault in California, NVT and LFEs [*Thomas et al*., 2009, 2012] occur at all phases of the tides and the maximum rate of occurrence coincides with the maximum tidal shear stress, as discussed in greater detail below.

[13] Observational studies substantiate prediction (2) that in regions of especially high tidal stress amplitude, a correlation of earthquakes with the tides is easier to detect [*Wilcock*, 2001]. *Wilcock* [2001] investigated a mid-ocean ridge environment where ocean tidal stress can be a magnitude larger than the solid earth tides and found a strong tidal correlation in a data set with only ~1500 events. In typical seismic catalogs of this size and much larger, there is no statistical correlation between the solid tides and earthquakes [*Vidale et al*., 1998; *Métivier et al*., 2009]. The same idea was employed by *Cochran et al*. [2004] who found a robust correlation between tidal stress and earthquakes in shallow subduction environments where the ocean tidal loads can be as large as 10 kPa and the confining stress is relatively low.

1.2. Tidal Modulation of Tremor on the San Andreas

[14] In contrast to shallow earthquakes which are quite insensitive to the tides except in cases of high-tidal amplitude, NVT and LFEs on the San Andreas near Parkfield are extremely sensitive to tidally induced shear stress changes with peak-to-peak amplitudes less than 0.5 kPa [*Thomas et al*., 2009; *Thomas et al*., 2012]. In Figure 1a, LFEs from April 2001 to February 2012 are binned according to the tidal right lateral shear stress on the SAF at the time of LFE occurrence. The number of events in each bin (N_{obs}) is normalized by the expected number of events (N_{exp}) assuming LFEs are randomly distributed in time. The expected number is the total number of events in the catalog divided by the total catalog time at that bin's range of tidal stress. $N_{obs}/N_{exp} > 1$ denotes an excess of LFEs at that stress level, and $N_{obs}/N_{exp} < 1$ indicates a deficit. Event occurrence rate varies systematically from low but nonzero at the lowest tidal stresses to high at the highest stress. NVT on the SAF shows the same relationship (see *Thomas et al*. [2009, Figure 3]). In contrast, LFEs show no strong or systematic relationship with the tides resolved as normal stress on the SAF (Figure 1b). Because the solid earth tidal strains are largely volumetric, the amplitude of the normal stress tide is more than ten times larger than the shear stress. That there is no strong normal stress effect is surprising but the absence may provide an additional constraint on faulting rheology.

[15] The only way for these collective observations to be explained by the laboratory-based model described above, for which the direct tidal load is not amplified by the modulation of fault creep surrounding earthquake sources, is if the effective normal stress is very low. However, calling upon arbitrarily low effective stress causes the model to fail when applied to the SAF LFE data [*Thomas et al*., 2011, 2012]. Predictions (2) and (3) cannot be simultaneously satisfied at low effective stress because the delay time decreases with effective normal stress. To produce the strong correlation seen on the deep SAF at tidal shear stresses of 0.4 kPa amplitude, the effective stress has to be so low that the delay time constant is of the order of the tidal period or shorter. Under those circumstances and natural rates of tectonic loading, earthquake occurrence will not occur at all phases of the tides, correlates with stressing rate rather than stress and is not in phase with the tidal stress [*Beeler and Lockner*, 2003]. It is unknown at present whether this lab model also fails to explain tidal modulation of NVT in Cascadia and elsewhere.

[16] In this study, we develop an alternative model to quantitatively explain the correlation between LFEs and NVT and

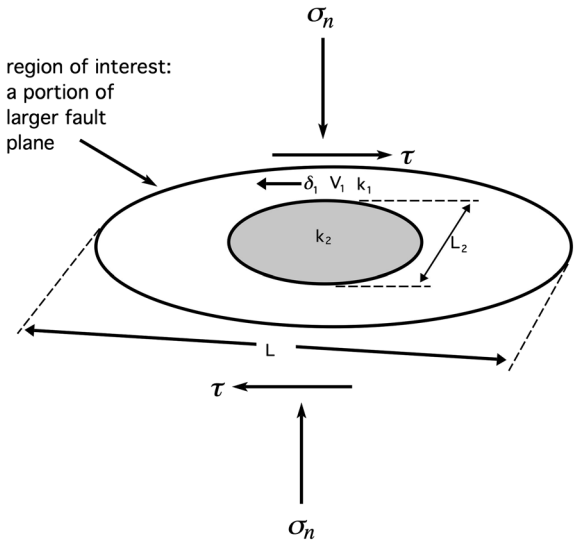

Figure 2. Schematic of the geometry of a low frequency earthquake source: a seismic patch of representative length L_2 embedded in an aseismically creeping fault plane of dimension L. Throughout the text of this paper, we refer to this patch surrounded by creep as the "region of interest." The stiffness of the region of interest is k (not labeled in the Figure). Slip, stiffness, and slip velocity of the creeping fault surrounding the patch are δ_1, k_1, and V_1, respectively. The patch stiffness is k_2.

the very low amplitude shear tides resolved onto the SAF at Parkfield using the model of *Shelly et al*. [2007a] described in the first paragraph of section 1. The model originates from earthquake fault mechanics studies that precede the discovery of nonvolcanic tremor, such as to describe shallow repeating earthquakes [*Bufe et al*., 1977; *Nadeau and Johnson*, 1998], and aftershocks [*Perfettini and Avouac*, 2004]. For this model, earthquake rates, rather than reflecting some intrinsic property of the earthquake source, can instead reflect the rate of aseismic creep of the surrounding fault [*Nadeau and Johnson*, 1998; *Perfettini and Avouac*, 2004], as we show in the following section for the SAF. Knowledge of the driving tidal stress changes can be used to determine whether particular mechanisms of fault creep (e.g., dislocation creep and low temperature plasticity) are physically plausible. We find for the creep mechanisms considered that the ambient shear resistance has to be of similar magnitude as the perturbation, precluding the mechanisms with creep strengths higher than kilopascal or tens of kilopascals.

2. Model of Deep Fault Slip and NVT

[17] According to *Shelly et al.'s* [2007a] model, an LFE is a brittle patch on a fault plane that is elsewhere and otherwise creeping (Figure 2). As shear stress has the strongest influence, we consider it in the greatest detail in this section. Constraints from normal stress are discussed briefly and separately in a subsequent section. In our representation (Figure 2), the portion of the fault plane of interest (the region of unsteady creep with an embedded LFE source) is subject to tectonic loading, stress from the tides, and unloading from slip: $\tau = \tau_{\text{tectonic}} + \tau_{\text{slip}} + \tau_{\text{tidal}}$, where we have assumed constant normal stress. Even though the LFE's only account for some of the tremor in the region [*Guilhem and Nadeau*, 2012], we ignore the existence of other tremor sources and any mechanical contributions they might make during loading. Shear stress on the fault plane from tectonic loading is $\tau_{\text{tectonic}} = k\delta_{\text{plate}}$, and k is the stiffness (MPa/micron) of the region of interest: both creeping portion of the fault and the patch itself. δ_{plate} is the loading displacement due to slip outside of the region of interest, i.e., tectonic loading in the Earth. The tides are represented using a body force consisting of simple oscillating component $\tau_{\text{tidal}} = \Delta\tau_{\text{tidal}} \sin(2\pi t/t_w)$ with shear stress amplitude $\Delta\tau_{\text{tidal}}$ and period t_w.

2.1. Loading of the Patch

[18] We focus on the stress on the fault patch as the patch is loaded to failure assuming it has a completely passive response to the imposed stresses until it fails. That is, its failure strength has no dependence on rate, time, or slip and remains completely locked until it fails at a particular level of stress. For laboratory failure, this is expected to be a good approximation at high stressing rates where the characteristic delay of friction [*Dieterich*, 1992, 1994] is short relative to the tidal period [e.g., *Beeler and Lockner*, 2003]. Stress concentrations that result in marginal yielding at asperity contacts [*Savage*, 2006; *Chen and Lapusta*, 2009] are ignored.

[19] The patch is loaded by tectonic forcing, by slip of the surrounding creeping portion of the fault and by the tides. In Appendix A, the relation for loading a stuck patch is derived and the shear stress on the patch is found to be

$$\tau_2 = k\left(\delta_{\text{plate}} - \delta_1\right) + k_2\delta_1 + \Delta\tau_{\text{tidal}} \sin(2\pi t/t_w), \qquad (1)$$

where k_2 is the patch stiffness and δ_1 is slip on the creeping portion of the fault. Some discussion of the application of equation 1 to 1-D and 2-D creeping fault geometries is also found in Appendix A, as are specific values of the stiffnesses k and k_2 for a plane strain example. The stressing rate for the patch is

$$\frac{d\tau_2}{dt} = kV_{\text{plate}} + V_1(k_2 - k) + \frac{2\pi\Delta\tau_{\text{tidal}}}{t_w} \cos(2\pi t/t_w). \qquad (2)$$

[20] Contrasting the two velocities in 2, V_{plate} is the plate rate, which is specified, whereas V_1 is the creep rate of the fault surrounding the patch. V_1 is stress dependent to a degree that depends on the particular creep rheology used. Because there are three sources of stress loading the patch, the rate of patch failure (LFE rate) is not a meter of the slip rate of the surrounding fault as has sometimes been assumed [e.g., *Shelly et al*., 2007a; *Ader et al*., 2012], except under special circumstances, as follows.

2.2. Seismicity Rate

[21] For threshold failure at constant normal stress, the failure rate is proportional to the shear stressing rate, provided that the stressing rate is positive [*Lockner and Beeler*, 1999]. For convenience and following ideas from *Dieterich* [1987, 1994] and *Lockner and Beeler* [1999], here, the seismicity rate R is defined relative to the background seismicity rate R_L associated with stressing from creep of the surrounding fault at constant rate, V_L, and tectonic loading of the patch at the plate rate:

$$\frac{R}{R_L} = \frac{\dot{\tau}}{\dot{\tau}_L} = \frac{kV_{\text{plate}}}{\left(kV_{\text{plate}} + [k_2 - k]V_L\right)} + \frac{V_1(k_2 - k)}{\left(kV_{\text{plate}} + [k_2 - k]V_L\right)} + \frac{2\pi\Delta\tau_{\text{tidal}}}{t_w\left(kV_{\text{plate}} + [k_2 - k]V_L\right)}\cos(2\pi t/t_w) \quad (3)$$

[22] Because the background creep rate may be episodic (nonconstant in time) V_L is defined as the long-term displacement-averaged creep rate. The details of the definition and its implications are found in Appendix B.

[23] Normalizing the earthquake rate 3 allows a natural connection with the observations of *Thomas et al*. [2012]. Recall that the data shown in Figure 1 define a histogram of earthquake occurrence for all events within all 88 LFE families identified on the deep SAF by *Thomas et al*. [2012]. $N_{\text{obs}}/N_{\text{exp}}$, is the actual number of events observed over the corresponding range of $\Delta\tau$, normalized by the expected number. Given that there is a particular duration of time spent at each stress range, the ratio of number of events $N_{\text{obs}}/N_{\text{exp}}$ is equivalent to the corresponding ratio of earthquake rates R/R_L over the time same range 3.

2.3. Conditions Where Seismicity Rate is Controlled by Fault Creep

[24] In this section, the conditions under which fault creep rather than tectonic loading or direct tidal loading dominates the seismicity rate are described. To establish the relative sizes of the three loading sources in 2, first consider the role of direct stressing from the tides. In the case the surrounding fault is creeping steadily at the plate rate, $V_1 = V_L = V_{\text{plate}}$ 3 becomes

$$\frac{R}{R_L} = 1 + \frac{2\pi\Delta\tau_{\text{tidal}}}{t_w k_2 V_{\text{plate}}}\cos(2\pi t/t_w). \quad (4a)$$

[25] The maximum contribution to the earthquake rate from the direct tidal stress, the second term on the right-hand side (RHS) of 4a, is its coefficient. For modulation due to direct tidal loading to be small compared to loading from fault creep is

$$k_2 >> \frac{2\pi\Delta\tau_{\text{tidal}}}{t_w V_{\text{plate}}}. \quad (4b)$$

[26] The observations suggest 4b is met for LFEs on the deep SAF. NVT [*Thomas et al*., 2009] and LFE occurrence [*Thomas et al*., 2012] are in phase with the tides for the shear stress resolved onto the SAF (Figure 1), meaning that the highest shear stresses are associated with the highest rates of earthquake occurrence. Because for threshold failure, earthquake occurrence from the tides themselves follows the stressing rate and be 90° out of phase with the tidal stress [*Lockner and Beeler*, 1999], the observations suggest that direct stressing is not important.

[27] That direct stressing from the tides is not an important LFE trigger is consistent with tremor source dimensions estimated by *Kao et al*. [2010] in Cascadia. *Kao et al*. [2010] obtained a radius of 13–30 m for M_w 2 and 1.5 tremor sources in Cascadia. *Kao et al*. estimated moment using a method that matches tremor amplitude to the amplitude of synthetic *S* waves, calibrated using local earthquakes. Source dimensions are then inferred by assuming slip of 1 cm. For tidal shear stress of 0.4 kPa, the daily tidal period of 12.4 h and $V_{\text{plate}} = 0.001$ μm/s (31 mm/yr), the quantity on the RHS of 4b is 56 MPa/m. Using an order of magnitude estimate for patch stiffness of G/L_2, a patch length of 20 m and $G = 30{,}000$ MPa, $k_2 \approx 1500$ MPa/m. However, using a more traditional method to determine earthquake source properties, *Fletcher and McGarr* [2011] estimate the radius of NVT sources on the SAF to be 200 to 560 m, in which case the left side of 4b is only slightly larger than the right. Note that both *Fletcher and McGarr* [2011] and *Kao et al.'s* [2010] estimates are for tremor bursts rather than individual LFEs, and presently the validity of assumptions 4b for LFEs is not constrained by data.

[28] The above estimates are a conservative upper limit on patch size because asperity contacts surrounded by creep are expected to undergo significant marginal slip as the stress is raised [*Savage*, 2006; *Chen and Lapusta*, 2009]. Because the contact margin is a region of stress concentration, slip in an annulus within the contact occurs well before failure of the asperity as a whole. At the time of failure, that portion of the patch slides in concert with the surrounding fault and the effective stiffness of the patch at failure is higher than if the entire patch remains stuck. The 3-D, fully dynamic calculations of *Chen and Lapusta* [2009] show that while marginal preseismic slip can reduce the effective size and increase the effective stiffness of asperities during nucleation, their coseismic extent can be large as the whole asperity. Thus, coseismic inferences of tremor source size [e.g., *Kao et al*., 2010; *Fletcher and McGarr*, 2011] may underestimate the stiffness appropriate for use in equation 3.

[29] An additional consideration in determining whether modulation due to direct tidal loading is small compared to loading due to creep at an average background rate involves the relative size of the background creep rate V_L to the plate rate V_{plate}. In equation 4b, the creeping portion of the fault was assumed to be steadily slipping at the plate rate. That actual LFE occurrence is episodic rather than continuous [*Shelly and Johnson*, 2011; *Thomas et al*., 2012] suggests that the fault creep rate is not steady, i.e., that the surrounding fault creeps at a rate larger than the plate rate for short periods of time and at rates lower than the plate rate during the intervening times, as described in Appendix B in the context of equation B1. These observations suggest that the displacement-averaged background creep rate $V_L >> V_{\text{plate}}$ and instead of 4b the requirement is $k + (k_2 - k)V_L/V_{\text{plate}} >> \frac{2\pi\Delta\tau_{\text{tidal}}}{t_w V_{\text{plate}}}$. The left-hand side contribution is dominated by $V_L\, k_2/V_{\text{plate}}$. For a patch with length 1120 m, the upper limit of *Fletcher and McGarr's* [2011] estimate, and V_L ten times larger than the plate rate, $V_L\, k_2/V_{\text{plate}} \approx 270$ MPa/s while the right-hand side is 4 to 5 times smaller. Thus, the observations of episodic LFE rates favor fault creep over direct tidal stress as the dominant source of stressing.

[30] Similarly, whether or not tectonic loading or fault creep dominates LFE stressing depends on the size of the patch relative to the surrounding fault. Again, assuming that the surrounding fault is creeping at the plate rate, using equation 3, the second term on the left-hand side dominates the stressing rate when $k_2 >> 2\,k$, equivalently when $L/L_2 >> 2$. Taking each of the 88 LFE sources to be isolated and $L_2 = 20$ m requires the dimension of the creeping region

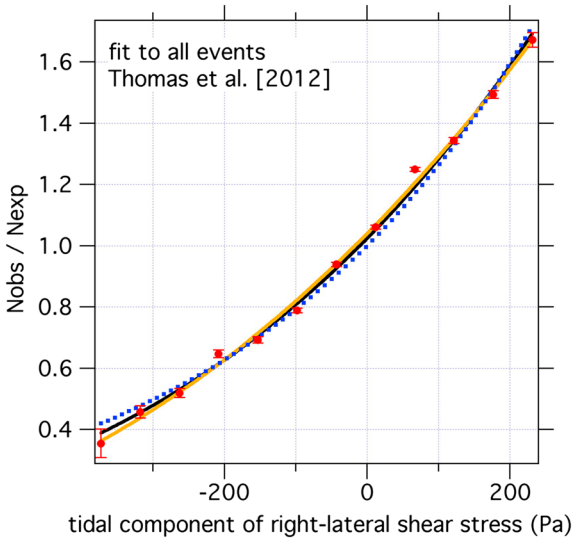

Figure 3. Data from *Thomas et al*. [2012] as shown in Figure 1a with fits to dislocation creep (equation (5); black), dislocation glide (equation (6); orange), and purely rate strengthening friction (equation (7); blue dashed).

around each patch to approach a hundred meters. If the creep rate is larger than the plate rate, as implied by LFE episodicity, the contribution of stressing from fault creep increases relative to that from tectonic loading, allowing creep loading to dominate for somewhat larger patches $L/L_2 >> 1 + V_{\text{plate}}/V_L$. This is not a large effect.

[31] There are no direct constraints on V_L for the SAF, so we conservatively assume that it is plate rate. So long as the LFE sources are on the order of tens of meters or less and $k_2 >> 2k$, and we have one of the principal implications of this model

$$\frac{R}{R_L} = \frac{\dot{\tau}}{\dot{\tau}_L} = \frac{N_{\text{obs}}}{N_{\text{exp}}} \approx \frac{V_1}{V_L} \tag{4c}$$

(also see *Ader et al*. [2012]). Figure 1 can equivalently be expressed as a plot of the normalized fault creep rate (Figure 3), and the fault patches that produce seismicity have an occurrence rate that directly reflects the rheological properties of the surrounding fault.

2.4. Relation Between Tidal Stress and Fault Creep Rate

[32] If the fault creep rheology is at steady state, as expected for ductile processes such as dislocation creep and also for rate-dependent friction under some circumstances (see below), then the tides will modulate the creep rate and the response of the fault to tidal stress changes can be used to estimate the rheological parameters of the flow law. Consider a nonspecific "viscous" fault zone, meaning, one whose strain rate or slip speed increases if the ambient stress or the tidal component of shear stress increases, $V_1 = f(\tau_1)$, where τ_1 is the shear stress in the creeping portion of the region of interest. In the following section, we adapt candidate flow laws for fault creep from the rock mechanics literature and put them in a form appropriate for changes in shear stress $\Delta\tau$ about a nominal value τ_0 which we associate with the background creep rate V_L, $V_1 = V_L f(\Delta\tau/\tau_0)$. The tidal stress amplitude $\Delta\tau$ is equated directly to fault creep strength, as has been done previously by *Ader et al*. [2012]. This is only strictly correct when the creeping portion of the fault experiences no elastic interactions due to fault slip anywhere within the region or the surroundings. If the fault creeps at steady state in the presence of tidal forcing, for example, from a single periodic component, the stress change about the nominal stress is just the tidal component of the stress $\Delta\tau = \Delta\tau_{\text{tidal}} \sin(2\pi t/t_w)$. The fault creep rate will be highest when the tidal stress is highest and exactly in phase with the tidal stress.

[33] Using this approach the tides modulate the creep rate by approximately 75% above the background rate (Figure 1). Inherent in this model-dependent inference is that the LFE patch size is 10's of meters or less, on the very lowest end of prior estimates from tremor bursts on the SAF and elsewhere [*Fletcher and McGarr*, 2011; *Kao et al*., 2010]. Also, while equation 4c was derived from consideration of a perfectly periodic tidal stress, so long as 4b and $k_2 >> 2k$ are met, 4c is general and can be applied regardless of the complexity of the tides.

3. Fault Rheologies

[34] Candidate deformation mechanisms for shearing of fault zones in the deep crust where there is sufficient laboratory data to constrain the rheology include rate-dependent friction, dislocation glide, and dislocation creep. Rate-dependent friction is the most often invoked mechanism of fault creep in the crust due to lab-demonstrated creep properties [e.g., *Moore and Rymer*, 2007; *Moore and Lockner*, 2007] and its ability to explain creep phenomenon such as afterslip [*Marone et al*., 1991] and slip-driven aftershock sequences [*Perfettini and Avouac*, 2004]. Dislocation glide is a plasticity mechanism that arises in materials that undergo dislocation motion at low temperature, for example,

Table 1. Rheological Parameters From Fits of LFE and Tidal Stress Data From *Thomas et al*. (2012) to Equations (5c), (6b) and (7b)

Rheology	Dislocation Creep	Dislocation Glide	Rate-Dependent Friction
Tremor weighted		$\tau_0 = 572 \pm 178$ Pa	
	$\beta = 0.92 \pm 0.07$	$Q_p/RT = -0.45 \pm 1.33$	
	$\tau_0 = 1152 \pm 149$ Pa	$\sigma_p = 882$ Pa ± 363	$a\sigma_e = 342 \pm 51$ Pa
Tremor unweighted		$\tau_0 = 617 \pm 255$ Pa	
	$\beta = 0.93 \pm 0.05$	$Q_p/RT = 0.18 \pm 1.75$	
	$\tau_0 = 1198 \pm 115$ Pa	$\sigma_p = 2{,}105 \pm 10610$ Pa	$a\sigma_e = 350 \pm 45$ Pa
LFEs		$\tau_0 = 971 \pm 317$ Pa	
	$\beta = 0.96 \pm 0.02$	$Q_p/RT = 0.56 \pm 1.54$	
	$\tau_0 = 1704$ Pa ± 83 Pa	$\sigma_p = 2{,}133$ Pa ± 302 Pa	$a\sigma_e = 464 \pm 48$ Pa
LFEs declustered		$\tau_0 = 1164 \pm 509$ Pa	
	$\beta = 0.97 \pm 0.02$	$Q_p/RT = 0.93 \pm 2.205$	
	$\tau_0 = 1890 \pm 87$ Pa	$\sigma_p = 2{,}446 \pm 878$ Pa	$a\sigma_e = 505 \pm 48$ Pa

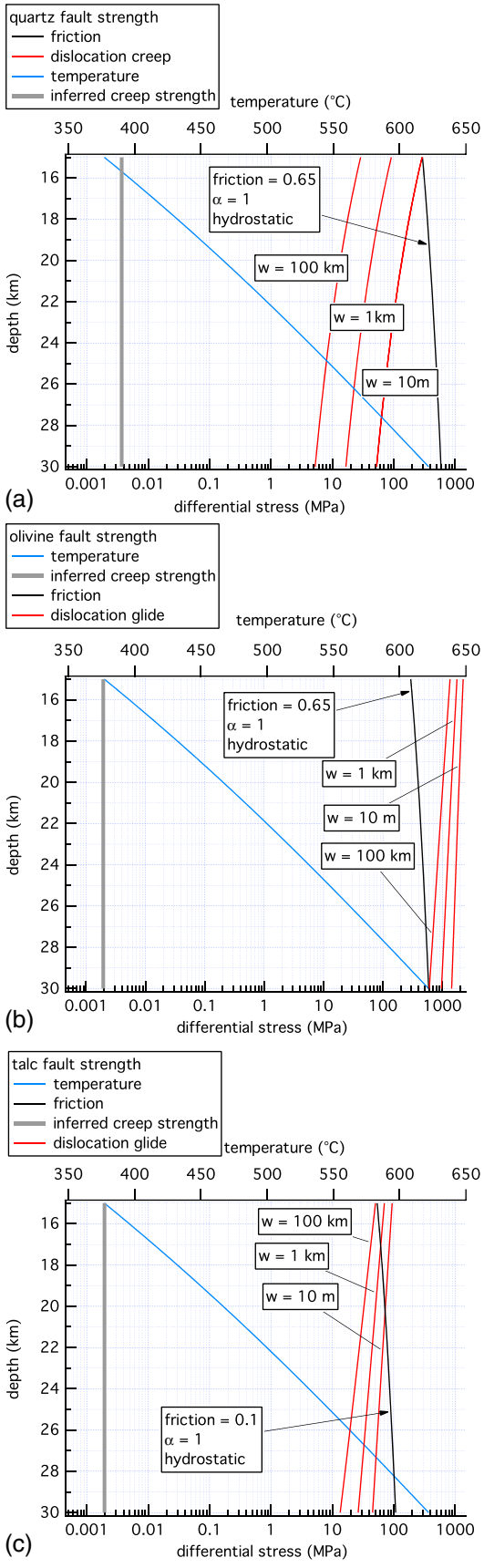

Figure 4

phyllosilicates (micas and clays), including talc [*Escartin et al.*, 2008] and other phases stable in the deep crust, notably olivine which deforms via dislocation creep at room temperature up to many hundreds of degrees [*Evans and Goetze*, 1979] For glide, dislocation climb is prevented at these temperatures due to kinetic or structural reasons. Dislocation creep arises at higher temperatures in olivine and also in most other silicates including quartz [*Evans*, 1984] but does not occur at high temperature in phyllosilicates [*Escartin et al.*, 2008]. We consider these three different fault rheologies in turn.

3.1. Power Law—Dislocation Creep

[35] Dislocation creep follows a power law rheology with the generic form

$$\dot{\varepsilon} = \dot{\varepsilon}_0 \beta \left(\frac{\sigma}{\sigma_0}\right)^n, \tag{5a}$$

where σ is the differential stress, β is a dimensionless constant, and $\dot{\varepsilon}_0$ is the strain rate at the background rate which we associate with the loading velocity V_L. The differential stress at the background strain rate is σ_0 and n is

Figure 4. The estimated shear strength of faults in the transition zone in a strike slip faulting environment. To estimate the stresses, we equate the mean stress, σ_m, the average of the greatest and least principal stresses, $(\sigma_1+\sigma_3)/2$, to the lithostatic load [e.g., *Townend and Zoback*, 2000]. In the shallow faulting regime, the fault effective normal stress $\sigma_e = \sigma_n - \alpha p$, for a fixed coefficient of friction μ, effective stress coefficient α, and an optimally oriented fault is $\sigma_e = (\sigma_m - \alpha p)\frac{\sin(\tan^{-1}\mu)\cos(\tan^{-1}\mu)}{\mu}$, and the fault differential stress for friction is $\sigma_\Delta = 2(\sigma_m - \alpha p)\sin(\tan^{-1}\mu)$. In the calculations shown $\alpha = 1$, pore pressure is hydrostatic (10 MPa/km), and the lithostat is 28 MPa/km. The resulting differential stress from friction is shown in black. Differential stress from the flow laws are shown in red at strain rates of 10^{-10}, 10^{-12}, 10^{-14}/s, which correspond to shear zone thicknesses of w = 10 m, 1 km, and 100 km, respectively. For flow due to dislocation glide or dislocation creep the fault differential strength is given by the flow law, equation (5) or (6) and the shear stress inferred from the data fit, is $\tau = \sigma_\Delta/2$. In blue is the temperature (top axis) estimated following *Lachenbruch and Sass*'s [1973] profile A for the San Andreas. (a) Quartz. The frictional strength (black) assumes μ = 0.65. The grey line is the inferred differential strength from the fit of equation (5) to the data, σ_Δ = 3.4 kPa. In red are predictions of the flow law equation (5) for strain rates of quartz using $n = 4$, $Q = 135$ kJ/mol, and $\dot{\varepsilon}_0/\sigma_0^4 = 1 \times 10^{-9}$/MPa^{4}s [*Hirth* personal communication, after *Hirth et al.*, 2001]. (b) Olivine. The frictional strength (black) assumes $\mu = 0.65$. The grey line is the inferred differential strength from the fit of equation (6b) to the data, $\sigma_\Delta = 1.9$ kPa. In red are predictions of the flow law equation (6a), $Q = 320$ kJ/mol, $\sigma_p = 5900$ MPa, and $\dot{\varepsilon}_0/\sigma_0^2 = 1.4 \times 10^{-7}$/MPa^{2}s [*Mei et al.*, 2010]. (c) Talc. The frictional strength (black) assumes $\mu = 0.1$. The grey line is the inferred differential strength from the fit of equation (6b) to the data, $\sigma_\Delta = 1.9$ kPa. In red are predictions of the flow law equation (6a) for talc using Q =166 kJ/mol, $\sigma_p = 377$ MPa, and $\dot{\varepsilon}_0/\sigma_0^2 = 0.08$/MPa^{2}s [*Hickman et al.*, 1997].

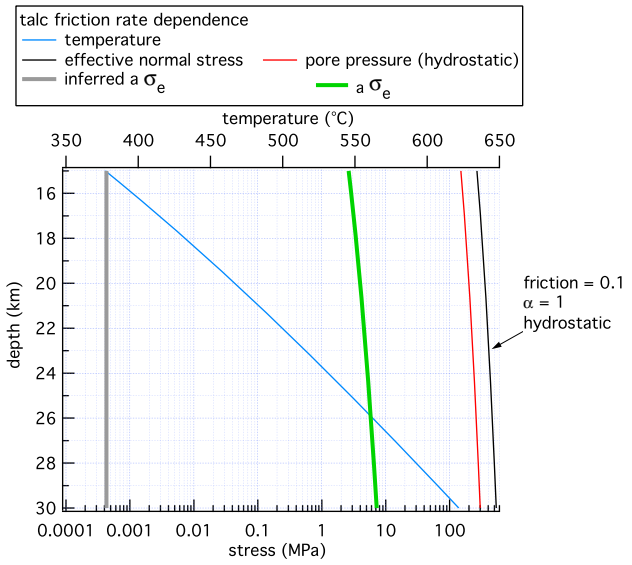

Figure 5. The effective normal stress and direct rate dependence of talc in the transition zone in a strike-slip faulting environment assuming hydrostatic fluid pressure. The stresses are calculated as described in the caption in Figure 4. The friction constitutive parameter a is assumed proportional to absolute temperature (see text) and has a depth-averaged value of ~0.011 over this range; the product $a\sigma_e$ is plotted in green. For comparison is the inferred value of $a\sigma_e$ from the fit to *Thomas et al.'s* [2012] LFEs using equation (7) (grey). Temperature (top axis) is shown in blue.

the stress exponent, expected to be between 3 and 6 for dislocation creep. Note that equation 5a uses different constants from the standard power law form. The flow law for dislocation creep is often written as $\dot{\varepsilon} = A\sigma^n \exp(-Q/RT)$ where A has dimensions of strain rate/stress^n [e.g., *Hirth et al*., 2001]. Our need to normalize the strain rate motivates the equivalent form 5a where the standard parameters are related by $A = \dot{\varepsilon}_0/\sigma_0{}^n$ and $\beta = \exp(-Q/RT)$, where Q is an activation energy, R is the gas constant, and T is absolute temperature.

[36] So long as the shear zone thickness is constant, as would be expected for steady state flow, then $\dot{\varepsilon}/\dot{\varepsilon}_0 = V/V_L$, as above, and for seismic failure of small brittle patches on a creeping fault plane

$$\frac{N_{\text{obs}}}{N_{\text{exp}}} = \frac{V}{V_L} = \beta\left(\frac{\sigma}{\sigma_0}\right)^n. \tag{5b}$$

[37] Differential stress is related to shear stress in the direction of shearing by a geometrical constant ($\tau = 0.5\sigma \sin 2\varphi$, where φ is the angle between the greatest principal stress and the fault zone), so the ratio $\sigma/\sigma_0 = \tau/\tau_0$. Defining $\Delta\tau = \tau - \tau_0$ as the deviation of shear stress from its nominal stress level τ_0, $\Delta\tau$ is the periodic (tidal) component of the shear stress, $\tau/\tau_0 = \Delta\tau/\tau_0 + 1$. The rheological equivalent of equation 5b for the data in Figure 1 is

$$\frac{N_{\text{obs}}}{N_{\text{exp}}} = \frac{V}{V_L} = \beta\left(\frac{\Delta\tau}{\tau_0} + 1\right)^n. \tag{5c}$$

[38] For dislocation creep, the power law exponent $n = 4$ is appropriate for quartz [*Hirth et al*., 2001]. The best fit value of β and the ambient shear stress are 0.9 and 1.7 MPa, respectively (Figure 3). The small uncertainties associated with the fit parameters are listed in Table 1.

3.2. Dislocation Glide

[39] Dislocation glide can be represented by the flow law

$$\dot{\varepsilon} = \dot{\varepsilon}_0\left(\frac{\sigma}{\sigma_0}\right)^2 \exp\left(\frac{-Q_p}{RT}\left[1 - \sqrt{\frac{\sigma}{\sigma_p}}\right]\right) \tag{6a}$$

(*Mei et al*. [2010], after *Kocks et al*. [1975] and *Frost and Ashby* [1982], where the reference strain rate and differential stress have the same interpretation as in 5b. σ_p is the Peierls stress, the yield strength at absolute zero. Q_p is activation energy at zero stress. Again replacing the ratio of differential stress to its reference value with the equivalent ratio of shear stress, replacing the differential stress with 2τ, and considering an imposed change yields

$$\frac{N_{\text{obs}}}{N_{\text{exp}}} = \frac{V}{V_L} = \left(\frac{\Delta\tau}{\tau_0} + 1\right)^2 \exp\left(\frac{-Q_p}{RT}\left[1 - \sqrt{\frac{2(\Delta\tau + \tau_0)}{\sigma_p}}\right]\right) \tag{6b}$$

for glide. The data in Figure 1 were fit with the flow law 6b resulting in $\tau_0 = 0.9$ MPa, $Q_p/RT = 0.5$, and $\sigma_p = 2$ MPa (Figure 4). Uncertainties in the parameters are listed in Table 1; these are small except for Q_p/RT which is very poorly constrained by these data.

3.3. Rate-Dependent Friction

[40] In room temperature experiments, rock friction is constant to first order; to second order friction depends on slip speed and "state" (slip rate, slip, and time dependences) [*Dieterich*, 1979; *Ruina*, 1983] such as represented by rate and state constitutive relations. While rate and state dependences determine the stability of sliding, they complicate analysis of stable fault creep which invariably arises when the direct rate dependence exceeds the state dependence (velocity strengthening). Accordingly, prior studies of afterslip and fault creep [*Marone et al*., 1991; *Perfettini and Avouac*, 2004; *Ader et al*., 2012] simplify the full rate and state equations by ignoring state; doing so is rigorously correct, for example, during sliding over short slip distances or sliding at steady state. More general neglect of state effects is appropriate for friction of some phyllosilicates such as muscovite and talc that lack a significant state dependence at room temperature [e.g., *Scruggs*, 1997; *Beeler*, 2007; *Beeler et al*., 2007]. For simplicity and other reasons detailed in section 4, we use talc as a representative phase for deep frictional slip on the SAF and assume purely rate dependent friction

$$\tau = \tau_0 + a\sigma_e \ln(V/V_L), \tag{7a}$$

where effective normal stress is σ_e, τ_0 is shear resistance at the nominal loading rate V_L, and a is a positive constant. Rearranging leads to

$$\frac{N_{obs}}{N_{\text{exp}}} = \frac{V}{V_L} = \exp\left(\frac{\Delta\tau}{a\sigma_e}\right) \tag{7b}$$

[*Beeler et al*., 2012; *Ader et al*., 2012]. For a fit of 7b, $a\sigma_e = 0.46$ MPa (Figure 5).

4. Discussion

[41] We compare the inferred rheological constants from the fits of the data (Figure 3) to independent laboratory measurements. To make direct comparisons, we use laboratory data from quartz, olivine, and talc. Quartz was selected because it is brittle in the shallow crust and is well studied in the frictional regime where it is quite strongly rate weakening when deformation is localized and not influenced by solution transport processes [*Chester*, 1995]. It deforms by dislocation creep in the deeper crust [*Hirth et al*., 2001] and it is among the most well-studied minerals at elevated temperature and pressure. The laboratory data for dislocation creep in quartz that constrains the flow law parameters are from temperatures in the range of 700 to 1100°C [*Hirth et al*., 2001] and strain rates on the order of 10^{-5}/s. Application to the transition zone on the SAF (T = 350–650°C, V = 0.001 μm/s) requires extrapolation to lower temperatures and strain rates. The friction data for quartz are extrapolated up significantly from room temperature and down slightly in slip rate.

[42] Olivine has a similar frictional strength to quartz but the underlying contact-scale deformation mechanisms are better understood [*Evans and Goetze*, 1979; *Boettcher et al*., 2007]. Low temperature plasticity operates in olivine at room temperature and extends to much greater temperatures than for quartz [*Evans and Goetze*, 1979], as does the frictional regime [*Boettcher et al*., 2007], and the flow behavior of olivine at high temperatures is well established [*Hirth and Kohlstedt*, 2003]. Data on low temperature plasticity and dislocation creep for olivine are from temperatures between room temperature and 1500°C [*Evans and Goetze*, 1979; *Hirth and Kohlstedt*, 2003] and need no temperature extrapolation. The strain rates are on the order of 10^{-5}/s and are extrapolated downward to transition zone rates. Olivine friction data are from 600 to 1000°C and are not extrapolated in temperature or in slip rate. Feldspar, which we do not consider in the present paper, has rheological properties that are intermediate [e.g., *Scholz*, 1990] and its behavior can reasonably be expected to be bounded by quartz and olivine.

[43] Talc is used to represent a material undergoing frictional creep. In the friction regime, it is among the very weakest materials [*Moore and Lockner*, 2004, 2007]. The SAF is thought to be as weak as talc by some researchers [*Zoback et al*., 1987] and talc is present in rock recovered from drilling [*Moore and Rymer*, 2007]. Talc's frictional properties are well described [*Scruggs*, 1997; *Morrow et al*., 2000; *Moore and Lockner*, 2004, 2007] and have a strong physical basis [e.g., *Morrow et al*., 2000; *Moore and Lockner*, 2004; *Beeler et al*., 2007]. The flow behavior is established over a limited range of conditions but it is not well studied or completely understood [*Hickman et al*., 1997; *Escartin et al*., 2008]. Talc dehydrates at a depth just below the tremor zone and may provide a source of fluid, widely thought to play a role in the physical properties of the transition zone. The choice of talc intends to represent the rheology of phyllosilicates that, while not well studied, are common in mature fault zones. Talc data used are from 25 to 900°C [*Edmond and Paterson*, 1971; *Hickman et al*., 1997; *Escartin et al*., 2008] and strain rates on the order of 10^{-5}/s. These were extrapolated in strain rate. The talc friction data are from room temperature to 400°C [*Scruggs*, 1997; *Moore and Lockner*, 2007] and need little extrapolation in temperature or slip rate.

[44] In the following subsections, we examine each of the possible mechanisms of fault creep, in turn, comparing the inferred parameters from the fits of each mechanism to *Thomas et al.'s* [2012] data to the experimentally determined parameters. With regard to measurement uncertainties in the laboratory parameters, the flow law parameter Q is liable to be good to ~10% [*Hirth et al*., 2001; *Hirth and Kohlstedt*, 2003] while the errors in friction rate dependence are generally considerably larger, being the same order as the measurement itself [e.g., *Moore and Lockner*, 2007].

4.1. Dislocation Creep

[45] Dislocation creep (5) provides a good fit to the observations. The inferred value of Q at the depth-averaged temperature of 505°C from the fit shown in Figure 3 is 0.26 kJ/mol ($Q = -RT\ln\beta$) compared to 135 kJ/mol [*Hirth et al*., 2001]. For other rock forming minerals, Q is of the same order, for example, for olivine $Q = 480 - 520$ kJ/mol, although olivine does not undergo dislocation creep at 500°C. Given the three order of magnitude difference in energy, dislocation creep can be eliminated as the controlling deformation mechanism for deep fault creep associated with NVT on the SAF. Similarly, the value of nominal differential stress required, $\sigma_0 \approx 3$ kPa, is too low to be plausible for quartz at these temperatures. Figure 4a shows the expected fault strength for dislocation creep on the SAF over the depth range of 15 to 30 km. The temperature profile is from *Blanpied et al*. [1995] for the SAF based on *Lachenbruch and Sass's* [1973] profile A. Values of τ_0 at strain rates of 10^{-10}, 10^{-12}, 10^{-14}/s are shown. These correspond to shear zone thicknesses of w = 10 m, 1 km, and 100 km, respectively. The conversion of strain rate to thickness $w = V_L/\dot{\varepsilon}$ uses the plate rate $V_L = V_{\text{plate}} = 0.001$ micron/s (31.6 mm/yr). As the weakest shear strength is associated with an implausible shear zone thickness and is more than three orders of magnitude higher than the fit to dislocation creep, this process can be eliminated to explain deep creep on the SAF. In addition, because of the large difference, the conclusion can be extended to include other typical quartzofeldspathic and likely all possible compositions of crustal rocks.

4.2. Dislocation Glide

[46] Solving for the inferred value of the activation energy from the fit of equation 7b shown in Figure 3 at the depth-averaged temperature of 505°C produces Q = 3.6 kJ/mol, while the experimentally measured value for olivine is Q = 523 kJ/mol [*Evans and Goetze*, 1979] to 320 kJ/mol [*Mei et al*., 2010]. For talc, the range inferred from *Hickman et al*. [1997] is 56 to 85 kJ/mol. The apparent activation energy for glide in silicates is on the order of many tens to many hundreds of kilojoules per mole [e.g., *Shea and Kronenberg*, 1992]. While the comparison suggests this mechanism does not control deep fault creep on the SAF, it cannot be eliminated because the uncertainty associated with the fit is much larger than Q/RT.

[47] A comparison of the inferred shear strength from the fit to the glide strength is more definitive. The inferred value of shear stress is 0.97 kPa and is of the same order as the tidal shear stresses themselves. Taking the differential stress to be twice the shear stress, the resulting 1.9 kPa is very low

relative to the differential stress of olivine (>500 MPa) at these conditions (Figure 4b). For talc, the estimated differential stress is greater than 10 MPa based on extrapolation of *Hickman et al*. [1997] and *Edmond and Paterson* [1971] (Figure 4c). Based on this comparison, glide can be ruled out as controlling fault creep on the deep SAF.

4.3. Rate-Dependent Friction

[48] For purely rate strengthening friction, $a\sigma_e = 0.46$ kPa. If the frictional parameter a for talc is controlled by low temperature plasticity, a increases in direct proportion to temperature [*Nakatani*, 2001; *Rice et al*., 2001], following a flow law of the form (6). Comparison of the friction rate dependence at room temperature $a = 0.0045$ with *Hickman et al.'s* [1997] rate dependence corrected for differences in stress and temperature shows good agreement [*Beeler et al*., 2007]. Extrapolating to the transition zone results in $a = 0.012$ for talc. Assuming hydrostatic fluid pressure, the depth-averaged effective normal stress is 400 MPa and $a\sigma_e = 4.8$ MPa for this depth range, four orders of magnitude higher than the fit to the tremor data (Figure 5). Thus, talc friction could control the rate dependence only if the effective normal stress is 40 kPa, much smaller than our hydrostatic assumption shown in Figure 5, and the pore pressure is lithostatic.

4.4. Summary of Constraints on Shear Stress From Fault Creep

[49] The reason dislocation creep and glide do not fit the observations with the expected rheological parameters is because the small tidal stresses produce a first order effect on the strain rate. That is only possible for these flow mechanisms for rock forming minerals if the stress perturbation is on the order of the ambient material shear strength τ_0. The failure of the ductile deformation mechanisms to represent the observations does indirectly imply that fault creep is controlled by friction, and that the shear stress in the region of fault creep is lower than the flow strength. Since for quartz and talc, the depth-averaged shear stress is on the order of 10 MPa to 100 MPa (Figures 4a and 4c), this is the upper bound on shear strength of the creeping portion of the deep San Andreas in this region. A possible lower bound comes from the fit with rate-dependent friction. Using $a\sigma_e = 0.46$ kPa with $a = 0.012$ and $\tau_0\sigma_e = 0.1$, the average shear resistance in this depth range would be ~4 kPa.

4.5. Constraints on Fluid Pressure and Shear Stress From the LFEs

[50] The existence of low-frequency earthquakes in the transition zone, when combined with the constraint on earthquake patch size from our analysis of fault creep, puts a lower limit on effective pressure in the source. Since LFEs produce stress drops that are sufficiently rapid to produce seismic displacements at the earth's surface, they are most easily explained by rate-weakening friction [*Dieterich*, 1979; *Ruina*, 1983]. Using the constraint on the maximum size of these events from our analysis of creep in the surrounding region, a minimum effective normal stress that allows for the existence of a length, $L_2 = 20$ m earthquakes, at these depths can be estimated. Taking the earthquake patch stiffness as $k_2 \approx G/L_2$, and the critical stiffness for instability to be $k_c = ((b\text{-}a)\ \sigma_e)/d_c$, the requirement for earthquake occurrence is

$$\sigma_e > \frac{d_c G}{(b-a)L_2}. \tag{8}$$

[*Dieterich*, 1979]. d_c, the slip weakening distance, and $(b-a)$, the rate dependence, are the fault patch's frictional properties. Quartz is strongly rate weakening at room temperature with $b-a$ between 0.002 and 0.004 [*Weeks et al*., 1991; *Chester*, 1995]. Using the arguments of temperature proportionality [*Nakatani*, 2001; *Rice et al*., 2001], this extrapolates to depth as $b-a = 0.0078$. For lab $d_c = 5$ μm, appropriate for a lower bound on σ_e, and $G = 30000$ MPa, the minimum effective pressure for earthquake occurrence is 0.96 MPa. This is more than an order of magnitude higher than required for fault creep to be controlled by friction. Unfortunately, quartz is unlikely to be rate weakening at these depths [*Chester*, 1995]. For olivine, which is known to be rate weakening up to 600°C, $b-a = 0.003$ [*Boettcher et al*., 2007], making the minimum effective pressure in 8, 2.5 MPa. So if friction controls fault creep and the occurrence of LFEs, significant material differences and differences in pore pressure between the creeping fault and the LFEs are required. The material difference is necessary to produce a change in sign of the rate dependence of friction from positive in the creeping region to negative in the seismic patches. The difference in pore pressure is required because the inferred effective normal stress of the creeping fault zone ($\sigma_e = 40$ kPa) is too low for the LFE patches to be unstable ($\sigma_e > 2.5$ MPa).

[51] Shear stress at LFEs is controlled presumably by olivine, feldspar, or similarly strong phase that is refractory at temperatures between 400 and 600°C, undergoing frictional sliding below the flow strength. The upper limit of shear strength for olivine is in the range of hundreds of megapascals (Figure 4). An approximate lower limit follows from 8, using a friction coefficient of 0.65, $\tau_0 = 1.6$ MPa.

4.6. Constraints From Tidal Normal Stress

[52] The normal stress changes from the tides resolved onto the SAF are approximately ten times larger than the shear stresses, yet they have less influence on LFE occurrence [*Thomas et al*., 2011]. This would seem to place significant constraints on the fault rheology. Unfortunately, they do not. Among the potential reasons that the relatively large tidal normal stresses would produce weak changes in LFE rate are (1) that fault creep is controlled by a ductile process that has no normal stress dependence, (2) that fault creep is controlled by friction but the pore pressure in the fault is undrained over the time scale of the tidal period [*Hawthorne and Rubin*, 2010], or (3) that fault creep is controlled by friction but the intrinsic friction coefficient is very small [*Thomas et al*., 2009]. Based on our analysis of the shear tides, we can eliminate (1) from consideration.

[53] For an undrained fault, (2), if the fault poroelastic properties are suitable, changes in fault normal stress may produce no change in effective normal stress. The relation between normal stress change and fault pore pressure is characterized by the Skempton coefficient $B = \mathrm{d}p/\mathrm{d}\sigma_m$, where σ_m is the mean stress. Laboratory faults are [*Brown and Scholz*, 1985], and shallow crustal faults are thought to be, highly anisotropic, being much more compliant normal to the fault [*Cocco and Rice*, 2002] than in plane. While it is uncertain whether or not faults at this depth are more compliant normal to the fault and whether the Skempton

coefficient is 1, under such conditions $B \approx \mathrm{d}p/\mathrm{d}\sigma_n$. Therefore, as long as $B \approx 1$, as it is in the shallow subsurface, any change in normal stress is exactly counterbalanced by an opposing change in pore pressure [see *Hawthorne and Rubin*, 2010]. Undrained conditions might be expected at this depth due to low permeability [*Manning and Ingebritsen*, 1999].

[54] With regard to (3), constraints on the intrinsic friction coefficient from the previous study of NVT on the SAF, *Thomas et al*. [2009] assumed that tremor occurrence reflects patch intrinsic properties, whereas in the present model, tremor occurrence reflects the intrinsic properties of the creeping fault surrounding the patch. Still, a similar constraint on fault friction coefficient arises in the present model. When normal stress changes are considered in the present model, there are more free parameters (fault friction, fault normal stress, patch normal stress, and a) to consider than a simple patch rate dependence coefficient. While there may be constraints on patch friction and ambient normal stress from this model, those are beyond the scope of the present study.

4.7. Limitations

[55] Significant limitations of the present study include temporal and spatial deficiencies of the 1-D approximation, and oversimplification of the fault creep behavior that result from the assumption of pure rate strengthening. Propagation and other spatial effects cannot be addressed with the present model. Observations of deep slip propagation rate and apparent propagation rate from NVT constrain the fault slip constitutive behavior [e.g., *Rubin*, 2011]. Furthermore, 1-D uniform slip models do not produce the temporal variation of fault strength during slow slip seen in 2 and 3 dimensioned simulations [*Hawthorne and Rubin*, 2010, 2014; *Segall and Bradley*, 2012]. The pure rate strengthening model assumed is unlikely to be strictly appropriate. Despite our experimental justification of this relationship for phyllosilicate friction at room temperature, even talc has a small evolution effect at 25°C that is apparently larger near the dehydration temperature [*Escartin et al*., 2008]. Deviations from pure rate strengthening may complicate interpretations of the relationship between earthquake occurrence and tidal stress [see *Perfettini et al*., 2003]. Furthermore, even the most reproducible measurements of friction rate dependence are uncertain and those made at elevated temperature and pressure on weak materials such as talc require corrections for jacketing and seal friction that further increase uncertainty [*Moore and Lockner*, 2007]. Finally, there is some physical basis for rate-dependent friction [*Nakatani*, 2001; *Rice et al*., 2001] that suggests the observed rate dependence results from contact-scale plasticity. These ideas can be used to extrapolate laboratory data, as we have done in the present study; however, they are theoretical constructs that have not been verified experimentally by contact-scale observations or other means.

[56] Separate limitations arise from assuming uniform slip over the creeping fault segments, zero slip within the asperity prior to failure, and no elastic interaction of the creeping portion of the fault with the surrounding region. Previous theoretical and numerical studies of faulting have shown that asperity failure induced by creep in the surroundings is preceded by slip inside the asperity adjacent to the creeping region. This occurs for true threshold failure [*Savage*, 2006] and for more complicated friction relations [*Chen and Lapusta*, 2009]. In 3-D simulations, the amount of marginal slip that occurs relative to the seismic slip and the size of the marginal region relative to asperity size both increase as the asperity gets smaller [*Chen and Lapusta*, 2009]. Thus, it is likely that seismic inferences of rupture size for tremor [*Fletcher and McGarr*, 2011; *Kao et al*. 2010] or for LFEs will overestimate the effective size of asperities at failure. Furthermore, our assumption of no slip within the asperity is incorrect and analysis using improved models of asperity failure is needed. In addition, even though we considered elastic interactions in determining the stressing rate at LFE sources (equation 2) and the rate of LFE occurrence (equations 3), in our separate analysis of creep rheologies, the tidal stresses are equated directly to the fault strength, ignoring any elastic effects. Slip within the creeping portion of the fault will tend to reduce the tidal stress amplitude there, reducing the stressing rate on LFE sources.

[57] Though episodic slip cannot occur for the purely rate strengthening friction at constant normal stress, such a model could be a valid approximation. Previous friction models of episodic slow slip are rate weakening at the plate rate [*Shibazaki and Iio*, 2003; *Segall et al*., 2010] but invariably rate strengthening at the highest slip speeds. The rate strengthening damps the slip rate to maintain subseismic slip rates. For a purely rate strengthening model 7a to be appropriate, the fault needs only to be purely rate strengthening about the representative loading velocity $V_L > V_{\mathrm{plate}}$. This could happen in a number of ways such as the long proposed relationship that leads to periodic slow slip [*Shibazaki and Iio*, 2003], rate, and state friction with a high speed cutoff on state [*Dieterich*, 1978]. Such behavior is observed sometimes at room temperature for fault slip on bare granite surfaces [*Okubo and Dieterich*, 1986; *Kilgore et al*., 1993] and has longstanding physical [*Dieterich*, 1978; *Estrin and Brechet*, 1996; *Nakatani, and Scholz*, 2006] and observational [*Okubo and Dieterich*, 1986; *Kilgore et al*., 1993; *Nakatani and Scholz*, 2004, 2006] basis, though it is unknown whether such behavior occurs at elevated temperature and pressure appropriate for deep slip. Another known way in which faults may become effectively rate strengthening at high sliding speed is a dilatancy-hardening mechanism used in models of deep slow slip by *Segall et al*. [2010]. Because there is no constraint on the loading velocity during episodic slip on the SAF, we have ignored the inconsistencies among the observations of tidally modulated LFE rates (Figure 1) which require rate strengthening creep, a purely rate strengthening model (7), and the episodic nature of LFE recurrence that seem to require accelerating slip rate.

[58] A closely related concern is if the fault creep rate is episodic, then, so long as the episodic behavior results from the rate dependence of the fault, it is likely that the onset of the episodes of accelerated creep is influenced by the tides, as they have shown to be in simulations of Cascadia slow slip by *Hawthorne and Rubin* [2014]. The implications of such behavior on the relation between the tidal stress and the LFE occurrence rate (Figure 1) have not been explored. For example, if the duration of slip episodes were very short relative to the tidal period, and if the onset of the episodes were stress sensitive, a systematic relation between LFE occurrence and the tides should arise that reflects tidal triggering of rapid slip rather than the tidally modulated slip model advocated in the present study. To explore the

consequences of this kind of behavior requires modeling of episodic creep with much more sophisticated approaches than have been used in the present study—3-D models of asperities [e.g., *Chen and Lapusta*, 2009], fault strength relations that produce episodic slip [*Segall and Bradley*, 2012; *Hawthorne and Rubin*, 2010, 2014], and analysis of the LFE catalog to determine episode duration.

[59] In addition, there are wide variations in the degree that individual LFE family occurrences are episodic [*Shelly and Johnson*, 2011] and in their tidal sensitivity [*Thomas et al*., 2011]. While our model explains the relationship between the tidal shear stresses and LFE occurrence on the San Andreas, this explanation is limited to the average behavior of LFEs and NVT depicted in Figure 1a and in *Thomas et al*. [2009, Figure 3]. Notably, single families can show a strong phase lag between the peak tidal shear stress and the maximum rate of occurrence [*Thomas et al*., 2012] that may be process symptomatic [e.g., *Ader et al*., 2012]. There are also spatial variations in tidal shear stress sensitivity. In addition, there are some LFE families that show systematic correlation with normal stress not evident in the collective.

5. Conclusions

[60] The occurrence rate of low-frequency earthquakes within nonvolcanic tremor on the deep extent of the San Andreas fault in central California shows strong systematic correlation with the daily solid earth tides resolved as shear stress in the direction of right-lateral slip on the fault [*Thomas et al*., 2012]. The rate of LFE occurrence is in phase with this tidal stress, the amplitude of the SAF shear stress tides is ~400 Pa and the rate of occurrence is modulated by 75%. This behavior can be well represented by a model in which the LFE sources are small seismic patches that fail at a threshold stress on an otherwise creeping fault plane. Seismic patches are loaded tectonically, directly by the tides and also by time-dependent creep of the surrounding fault. For a background creep rate V_L approximately equal to the plate rate V_{plate}, fault creep dominates LFE occurrence so long as the LFE source is tens of meters or smaller, but for a larger $V_L \approx 10 V_{\text{plate}}$, fault creep would dominate for patch sizes hundreds of meters or smaller. Under these restrictive conditions, the model-predicted LFE rate is proportional to the fault creep rate.

[61] Using the observed occurrence data, the model can constrain the rheological properties of the creeping fault, essentially by equating the occurrence rate versus tidal stress data to a strain rate versus stress relationship and fitting that data with candidate rheologies. Ductile processes, dislocation creep and dislocation glide, are not consistent with the observed fault creep in the source region of NVT. These processes require nominal flow strength on the order of the tidal stress to produce the observed strongly modulated occurrence rate, and laboratory observed flow strengths are higher by orders of magnitude for a wide range of possible fault materials and conditions. Purely rate dependent friction can be consistent with the observations but only if the product of the friction rate dependence and effective normal stress is approximately 0.5 kPa. For talc, the friction rate dependence extrapolated to this depth is about 0.01 which we take to be typical for frictional creep of phyllosilicates in the deep crust. Thus, to explain the inference with talc requires the effective normal stress to be ~50 kPa. Were effective normal stress this low, and friction controlled by talc, the SAF shear resistance would be ~ 4 kPa.

[62] Given the failure of ductile rheologies to explain the observations, the lack of laboratory studies of faulting in the presence of pore fluid at the temperature and pressures of the transition zone and the extremely low inferred shear stress, our conclusion that friction controls fault creep is one that is not verified experimentally and will be difficult to verify. Nevertheless, if the LFE source is as small as 20 m, temperature extrapolated friction properties require that the minimum effective pressure at the LFE source is ~ 2.5 MPa. Provided that laboratory-like friction controls both fault creep and seismicity, our application of these friction models to fault creep and earthquake occurrence requires both material contrasts and differences in effective stress between the creeping and seismic parts of the fault.

[63] The weak correlation between the normal stress component of the tides and LFE occurrence is not explained by our work, despite the amplitude of the tidal normal stress being approximately 10 times the shear stress that strongly correlates. For this model, assuming rate-dependent friction, there may be too many free parameters to produce constraints. There likely are hydraulic/poroelastic phenomena that reduce the sensitivity to normal stress at these depths as argued originally by *Hawthorne and Rubin* [2010] for deep tremor in Cascadia.

Appendix A: Asperity Model

[64] To represent the stress transfer from tectonic loading, fault creep, and tidal stresses to a seismic patch on a plate bounding fault such as the San Andreas, we use an elastic fault model. The derivation uses plane strain geometry; however, the form of the resulting equation for stress on the patch is more general with application to antiplane strain and also to some simple 2-D fault geometries. The region of interest is a fault segment that is creeping about an embedded seismic asperity (Figure 1). The region of interest with dimension L is partitioned into a central patch of dimension L_2, and two creeping regions on either side of the patch of dimension $(L - L_2)/2$ (Figure A1). Slip within in each of the three regions is uniform, and the two creeping regions slip the same amount. The stiffness of the patch and region of interest are $k_2 = 2G/[\pi(1-\nu)L_2]$ and $k = 2G/[\pi(1-\nu)L]$, respectively. The stress on the patch, τ_2, results from three sources: an imposed tectonic stress due to slip on the fault that occurs outside the region of interest, τ_{tectonic}, stress from fault slip within the region of interest, τ_{slip}, and stress from the tides τ_{tidal},

$$\tau_2 = \tau_{\text{tectonic}} + \tau_{\text{slip}} + \tau_{\text{tidal}}. \tag{A1}$$

[65] The tectonic stress is $\tau_{\text{tectonic}} = k\delta_{\text{plate}}$, where δ_{plate} is the loading displacement due to motion along the plate boundary $\delta_{\text{plate}} = V_{\text{plate}}\, t$, and t and V_{plate} are time and the plate motion rate, respectively. For a fault segment i, the stress contribution from slip from all segments is

$$\tau_i = S_{ij}\delta_j, \tag{A2}$$

where there is summation over $j = 1$ to N; N is the total number of segments and

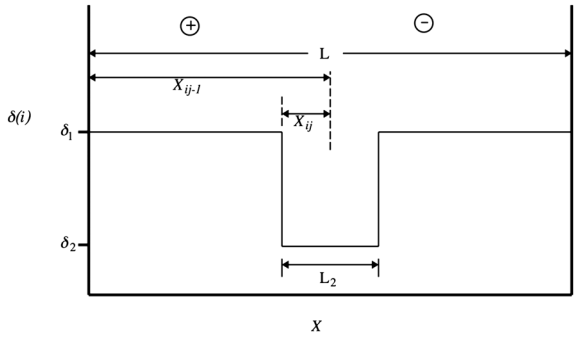

Figure A1. Schematic diagram of the distribution of slip within a fault region of dimension L, consisting of three dislocation segments: a central stuck patch of dimension L_2 and slip δ_2 and two adjacent creeping regions of dimension $L/2 - L_2/2$ and slip δ_1. Distances used to define coefficients in the stiffness matrix S_{ij} (equation A2) are labeled for the case where segment i is the central stuck segment and j is the left slipped segment.

$$S_{ij} = \frac{G}{2\pi(1-\nu)}\left[\frac{1}{X_{ij}} - \frac{1}{X_{ij-1}}\right],$$

[*Weertman*, 1979; *Dieterich*, 1992]. X_{ij} and X_{ij-1} are the distances from the center of segment i to the right and left edges of segment j, respectively (Figure A1). The distances X are positive as measured to the left from the center of segment i, and negative to the right. For the patch, the stress contribution from fault slip comes from slip of the two creeping segments, δ_1, and from self-slip, δ_2

$$\tau_{\text{slip}} = \frac{G}{2\pi(1-\nu)}\left[\left(\frac{2}{L_2} - \frac{2}{L}\right)\delta_1 + \left(-\frac{2}{L_2} - \frac{2}{L_2}\right)\delta_2 + \left(\frac{2}{L_2} - \frac{2}{L}\right)\delta_1\right]. \tag{A3}$$

[66] Combining terms and rewriting using the region of interest and patch stiffnesses, the contribution of stress change due to fault slip in the region of interest is $\tau_{\text{slip}} = -k\delta_1 + k_2(\delta_1 - \delta_2)$. Using the appropriate values for the stiffnesses, this expression for stress change on the patch due to slip within the region of interest is general and applies, for example, exactly to the 2-D geometry of a circular patch surrounded by a larger circular creeping region shown in Figure 1, as well as to other simple 2-D geometries (Allan Rubin, unpublished analysis).

[67] Stress on the patch is

$$\tau_2 = k\left(\delta_{\text{plate}} - \delta_1\right) + k_2(\delta_1 - \delta_2) + \tau_{\text{tidal}}. \tag{A4}$$

We consider stress transfer during loading to failure while the fault patch is stuck, so $\delta_2 = 0$. The tidal stresses on the patch are body forces and therefore can be applied directly rather than through an elastic element. In our initial analysis, these are idealized to be perfectly periodic, $\tau_{\text{tidal}} = \Delta\tau_{\text{tidal}} \sin(2\pi t/t_w)$ where $\Delta\tau_{\text{tidal}}$ and t_w are the amplitude and period of the tide. The complete expression for stress of the stuck patch is

$$\tau_2 = k\left(\delta_{\text{plate}} - \delta_1\right) + k_2\delta_1 + \Delta\tau_{\text{tidal}} \sin(2\pi t/t_w). \tag{A5}$$

Appendix B: The Background Creep Rate, V_L

[68] The seismicity rate of the asperity model has a background creep rate, V_L. This creep rate may be the long-term, time-averaged creep rate of the San Andreas, V_{plate} but because LFE occurrence is episodic, V_L is likely to be an accelerated rate $V_L > V_{\text{plate}}$. To allow for this range of possible rates, we define V_L as the long-term, displacement-averaged creep rate

$$V_L = \frac{1}{D}\int_0^D V_1 \mathrm{d}\delta_1, \tag{B1}$$

where D is the total amount of creep. Distinguishing between V_{plate} and V_L is important because it is possible, even likely, that most LFEs occur at times of elevated creep rate, such as for nonvolcanic tremor associated with deep episodic slip in Cascadia, and what we are likely observing in the seismicity rate is tidal modulation of that elevated creep rate. That is, for example, if the plate rate were 12 mm/yr but the creep rate followed an unsteady, stick-slip, periodic pattern of zero for 29.4 days followed by 1 day of creep at a constant rate of 1 mm/day, the time-averaged creep rate would be exactly the plate rate, 12 mm/yr, while the appropriate loading rate from creep would be $V_L = 1$ mm/day, more than 30 times greater than the plate rate. In such cases where the creep rate is episodic, the higher-loading rate given by B1 is appropriate because we are examining tidal modulation around the mean slip rate when tremor is occurring.

Appendix C: Rheological Parameters for Low-Frequency Earthquakes and Nonvolcanic Tremor on the San Andreas

[69] In addition to the fits of the *Thomas et al*. [2012] catalog to each of the candidate rheologies, as described in the text, section **3**, we also conducted fits to the NVT catalog of *Nadeau and Guilhem* [2009]. The fits to tremor show that our conclusions about LFE triggering by the tides may be general and perhaps the approach developed in this study could be used in other tectonic regions where detailed LFE data sets are not available. Furthermore, we fit the candidate rheologies to crudely declustered versions of the LFE and NVT catalogs to demonstrate that the result is not affected by clustering. The 88 LFE families have interevent times between 152 days and 4 s. Since the LFEs by definition are colocated and most families have average interevent times that range from 0.18 days, for the shallow families that occur as part of slip episodes [*Thomas et al*., 2012], to 1.34 days in the deeper, more continuous families, traditional declustering methods that rely on space-time distributions of seismicity [e.g., *Gardner and Knopoff*, 1974] would exclude the vast majority of the catalog. We also acknowledge that "bursts" of events like those described in *Shelly and Hardebeck* [2010] may bias the tidal correlation toward greater values. We decluster the LFE catalog by removing all events with recurrence times less than 15 min. This choice is somewhat arbitrary, however, it allows us to filter out all but the first events in LFE bursts while retaining events that occur within slip episodes with an average of ~30 min recurrence intervals. Filtering in this way reduces the number of events in the catalog by a factor of four. We also analyze weighted and unweighted NVT catalogs. In the unweighted version,

all tremor events are weighted equally while in the alternate version, each event is weighted by its duration which ranges from 3 to 20 min. Best fitting parameters for the four rheologies considered are shown in Table 1.

[70] **Acknowledgments.** NMB greatly benefited from an ongoing dialogue about triggering of earthquakes with David Lockner and another on deep slip and NVT with Evelyn Roeloffs and Wendy McCausland. Noel Bartlow suggested that NVT sources obey a threshold failure relation. Declustering the LFE catalog by AMT was done in response to comments made by Jeanne Hardebeck. Greg Hirth provided guidance on ductile flow laws and related topics and on phyllosilicates and their mechanical properties. This paper was greatly improved in response reviews by Jim Savage, David Lockner, Allan Rubin, an anonymous referee, and the JGR Associate Editor. During the review stage, Allan Rubin suggested the particular form of the equation for patch stressing rate 2 and corrected an error in the seismicity rate equation 3 used in the published version of this study.

References

Ader, T. J., J.-P. Ampuero, and J.-P. Avouac (2012), The role of velocity-neutral creep on the modulation of tectonic tremor activity by periodic loading, *Geophys. Res. Lett.*, *39*, L16310, doi:10.1029/2012GL052326.

Audet, P., M. G. Bostock, N. I. Christensen, and S. M. Peacock (2009), Seismic evidence for overpressured subducted oceanic crust and megathrust fault sealing, *Nature*, *457*, 76–78, doi:10.1038/nature07650.

Beeler, N. M. (2007), Laboratory-observed faulting in intrinsically and apparently weak materials: Strength, seismic coupling, dilatancy, and pore fluid pressure, in *The Seismogenic Zone of Subduction Thrust Faults*, edited by T. Dixon and C. Moore, pp. 370–449, Columbia Univ. Press, New York.

Beeler, N. M., and D. A. Lockner (2003), Why earthquakes correlate weakly with Earth tides: The effects of periodic stress on the rate and probability of earthquake occurrence, *J. Geophys. Res.*, *108*(B8, 2391), doi:10.1029/2001JB001518.

Beeler, N. M., T. E. Tullis, A. K. Kronenberg, and L. A. Reinen (2007), The instantaneous rate dependence in low temperature laboratory rock friction and rock deformation experiments, *J. Geophys. Res.*, *112*, B07310, doi:10.1029/2005JB003772.

Beeler, N. M., A. Thomas, R. Burgmann, and D. Shelly (2012), Modulation of tectonic tremor by the tides: Physical models descended from Leon Knopoff with application to the deep San Andreas, *Seismol. Res. Lett.*, *82*, 330.

Blanpied, M. L., D. A. Lockner, and J. D. Byerlee (1995), Frictional slip of granite at hydrothermal conditions, *J. Geophys. Res.*, *100*, 13,045–13,064.

Boettcher, M. S., G. Hirth, and B. Evans (2007), Olivine friction at the base of the oceanic seismogenic zones, *J. Geophys. Res.*, *112*, B01205, doi:10.1029/2006JB004301.

Brown, S. R., and C. H. Scholz (1985), The closure of random elastic surfaces in contact, *J. Geophys. Res.*, *90*, 5531–5545.

Bufe, C. G., P. W. Harsh, and R. O. Burford (1977), Steady-state seismic slip – A precise recurrence model, *Geophys. Res. Lett.*, *4*, 91–94.

Chen, T., and N. Lapusta (2009), Scaling of small repeating earthquakes explained by interaction of seismic and aseismic slip in a rate and state fault model, *J. Geophys. Res.*, *114*, B01311, doi:10.1029/2008JB005749.

Chester, F. M. (1995), A rheologic model for wet crust applied to strike-slip faults, *J. Geophys. Res.*, *100*, 13,033–13,044.

Cocco, M., and J. R. Rice (2002), Pore pressure and poroelasticity effects in Coulomb, stress analysis of earthquake interactions, *J. Geophys. Res.*, *107*(B2, 2030), doi:10.1029/2000JB000138.

Cochran, E. S., J. E. Vidale, and S. Tanaka (2004), Earth tides can trigger shallow thrust fault earthquakes, *Science*, *306*, 1164–1166.

Dieterich, J. H. (1978), Time-dependent friction and the mechanics of stick slip, *Pure Appl. Geophys.*, *116*, 790–806.

Dieterich, J. H. (1979), Modeling of rock friction: 1. Experimental results and constitutive equations, *J. Geophys. Res.*, *84*, 2161–2168, doi:10.1029/JB084iB05p02161.

Dieterich, J. H. (1987), Nucleation and triggering of earthquake slip: Effect of periodic stresses, *Tectonophysics*, *144*, 127–139.

Dieterich, J. H. (1992), Earthquake nucleation on faults with rate- and state-dependent strength, in *Earthquake Source Physics and Earthquake Precursors*, edited by T. Mikumo et al., pp. 115–134 , Elsevier, New York.

Dieterich, J. H. (1994), A constitutive law for rate of earthquake production and its application to earthquake clustering, *J. Geophys. Res.*, *99*, 2601–2618.

Edmond, J. M., and M. S. Paterson (1971), Strength of solid pressure media and implications for high pressure apparatus, *Contrib. Mineral. Petrol.*, *30*, 141–160.

Escartin, J., M. Andreani, G. Hirth, and B. Evans (2008), Relationships between the microstructural evolution and the rheology of talc at elevated pressures and temperatures, *Earth Planet. Sci. Lett.*, *268*, 463–475.

Estrin, Y. and Y. Brechet (1996), On a model of frictional sliding, *Pure Appl. Geophys.*, *4*, 745–762.

Evans, B. (1984), The effect of temperature and impurity content on indentation hardness of quartz, *J. Geophys. Res.*, *89*, 4213–4222.

Evans, B., and C. Goetze (1979), The temperature variation of hardness of olivine and its implication for polycrystalline yield stress, *J. Geophys. Res.*, *84*, 5505–5524.

Fletcher, J. B., and A. McGarr (2011), Moments, magnitudes, and radiated energies of non-volcanic tremor near Cholame, CA, from ground motion spectra at UPSAR, *Geophys. Res. Lett.*, *38*, L16314, doi:10.1029/2011GL048636.

Frost, H. J., and M. F. Ashby (1982), *Deformation Mechanism Maps*, 167 pp., Pergamon, New York.

Gardner, J. K., and L. Knopoff (1974), Is the sequence of earthquakes in Southern California, with aftershocks removed, Poissonian?, *Bull. Seismol. Soc. Am.*, *64*, 1363–1367.

Ghosh, A., J. E. Vidale, Z. Peng, K. C. Creager, and H. Houston (2009), Complex nonvolcanic tremor near Parkfield, California, triggered by the great 2004 Sumatra earthquake, *J. Geophys. Res.*, *114*, B00A15, doi:10.1029/2008JB006062.

Gomberg, J., J. L. Rubinstein, Z. Peng, K. C. Creager, J. E. Vidale, and P. Bodin (2008), Widespread triggering of nonvolcanic tremor in California, *Science*, *319*, 173, doi:10.1126/science.1149164.

Guilhem, A., and B. Nadeau (2012), Episodic tremors and deep slow-slip events in central California, *Earth Planet. Sci. Lett.*, *357/358*, 1–10.

Hawthorne, J. C., and A. M. Rubin (2010), Tidal modulation of slow slip in Cascadia, *J. Geophys. Res.*, *115*, B09406, doi:10.1029/2010JB007502.

Hawthorne, J. C., and A. M. Rubin (2014), Tidal modulation and back-propagating fronts in slow slip events simulated with a velocity weakening to -strengthening friction law, *J. Geophys. Res. Solid Earth*, *118*, 1216–1239, doi:10.1002/jgrb.50107.

Heaton, T. H. (1982), Tidal triggering of earthquakes, *Bull. Seismol. Soc. Am.*, *72*, 2181–2200.

Hickman, J. B., E. N. Zhurina, and A. K. Kronenberg (1997), Deformation of talc and pyrophyllite: Disruption of van der Waals bonds and comparisons with calculated interlayer forces, *Eos Trans. AGU*, *78*, Fall Meet. Suppl., F724.

Hill, D. P. (2010), Surface-wave potential for triggering tectonic (nonvolcanic) tremor, *Bull. Seismol. Soc. Am.*, *100*, 1859–1878, doi:10.1785/0120090362.

Hirth, G., and D. Kohlstedt (2003), Rheology of the upper mantle and mantle wedge: A view from the experimentalists, in *Inside the Subduction Zone Factory*, Geophys. Monogr. Ser., *138*, 83–105, AGU, Washington, D. C.

Hirth, G., C. Teyssier, and W. J. Dunlap (2001), An evaluation of quartzite flow laws based on comparisons between experimentally and naturally deformed rocks, *Int. J. Earth Sci.*, *90*, 77–87.

Ide, S., G. C. Beroza, D. R. Shelly, and T. Uchide (2007a), A scaling law for slow earthquakes, *Nature*, *447*, 76–79, doi:10.1038/nature05780.

Ide, S., D. R. Shelly, and G. C. Beroza (2007b), Mechanism of deep low frequency earthquake: Further evidence that deep nonvolcanic tremor is generated by shear slip on the plate interface, *Geophys. Res. Lett.*, *34*, L03308, doi:10.1029/2006GL028890.

Kao, H., S.-J. Shan, H. Dragert, G. Rogers, J. F. Cassidy, and K. Ramachandran (2005), A wide depth distribution of seismic tremors along the northern Cascadia margin, *Nature*, *436*, 841–844, doi:10.1038/nature03903.

Kao, H., K. Wang, H. Dragert, J. Y. Kao, and G. Rogers (2010), Estimating seismic moment magnitude (Mw) of tremor bursts in northern Cascadia: Implications for the "seismic efficiency" of episodic tremor and slip, *Geophys. Res. Lett.*, *37*, L19306, doi:10.1029/2010GL044927.

Kilgore, B. D., M. L. Blanpied, and J. H. Dieterich (1993), Velocity dependent friction of granite over a wide randge of conditions, *Geophys. Res. Lett.*, *20*, 903–906.

Klaus, A. J., K. C. Creager, J. R. Sweet, and A. G. Wech, (2011), Space time variations in tidal stress and Cascadia tremor amplitude, Abstract S23B–2246, AGU Fall Meeting.

Knopoff, L. (1964), Earth tides as a triggering mechanism for earthquakes, *Bull. Seismol. Soc. Am.*, *54*, 1865–1870.

Kocks, U. F., A. S. Argon, and M. F. Ashby (1975), *Thermodynamics and Kinetics of Slip*, 291 pp., Pergamon, Oxford.

Lachenbruch, A. H., and J. H. Sass (1973), Thermo-mechanical aspects of the San Andreas fault system, in *Proceedings of the Conference on the Tectonic Problems of the San Andreas Fault System*, pp. 192–205, Stanford University Press, Stanford, Calif.

Lambert, A., H. Kao, G. Rogers, and N. Courtier (2009), Correlation of tremor activity with tidal stress in the northern Cascadia subduction zone, *J. Geophys. Res.*, *114*, B00A08, doi:10.1029/2008JB006038.

Lockner, D. A., and N. M. Beeler (1999), Premonitory slip and tidal triggering of earthquakes, *J. Geophys. Res.*, *104*, 20,133–20,151.

Manning, C., and S. Ingebritsen (1999), Permeability of the continental crust: Implications of geothermal data and metamorphic systems, *Rev. Geophys.*, *37*, 127–150.

Marone, C., C. H. Scholz, and R. Bilham (1991), On the mechanics of earthquake afterslip, *J. Geophys. Res.*, *96*, 8441–8452.

Mei, S., A. M. Suzuki, D. L. Kohlstedt, N. A. Dixon, and W. B. Durham (2010), Experimental constraints on the strength of the lithospheric mantle, *J. Geophys. Res.*, *115*, B08204, doi:10.1029/2009JB006873.

Métivier, L., O. de Viron, C. Conrad, S. Renaul, M. Diament, and G. Patau (2009), Evidence of earthquake triggering by the solid earth tides, *Earth Planet. Sci. Lett.*, *278*, 370–375.

Miyazawa, M., and E. E. Brodsky (2008), Deep low-frequency tremor that correlates with passing surface waves, *J. Geophys. Res.*, *113*, B01307, doi:10.1029/2006JB004890.

Moore, D., and D. A. Lockner (2004), Crystallographic controls on the frictional behavior of dry and water-saturated sheet structure minerals, *J. Geophys. Res.*, *109*, B03401, doi:10.1029/2003JB002582.

Moore, D. E., and D. A. Lockner (2007), Friction of the smectite clay montmorillonite: A review and interpretation of data, in *The Seismogenic Zone of Subduction Thrust Faults*, edited by T. Dixon and C. Moore, pp. 317–345, Columbia Univ. Press, New York.

Moore, D., and M. Rymer (2007), Talc-bearing serpentinite and the creeping section of the San Andreas fault, *Nature*, *448*, 795–797, doi:10.1038/nature06064.

Morrow, C. A., D. E. Moore, and D. A. Lockner (2000), The effect of mineral bond strength and adsorbed water on fault gouge frictional strength, *Geophys. Res. Lett.*, *27*, 815–818.

Nadeau, R. M., and A. Guilhem (2009), Nonvolcanic tremor evolution and the San Simeon and Parkfield, *Science*, *325*, 191–194, doi:10.1126/science.1174155.

Nadeau, R. M., and L. R. Johnson (1998), Seismological studies at Parkfield VI: Moment release rates and estimates of source parameters for small repeating earthquakes, *Bull. Seismol. Soc. Am.*, *88*, 790–814.

Nakata, R., N. Suda, and H. Tsuruoka (2008), Non-volcanic tremor resulting from the combined effect of Earth tides and slow slip events, *Nat. Geosci.*, *1*, 676–678, doi:10.1038/ngeo288.

Nakatani, M. (2001), Conceptual and physical clarification of rate and state friction: Frictional sliding as a thermally activated rheology, *J. Geophys. Res.*, *106*, 13,347–13,380.

Nakatani, M., and C. H. Scholz (2004), Frictional healing of quartz gouge under hydrothermal conditions: 1. Experimental evidence for solution transfer healing mechanism, *J. Geophys. Res.*, *109*, doi:10.1029/2001JB001522.

Nakatani, M., and C. H. Scholz (2006), Intrinsic and apparent short-time limits for fault healing: Theory observations and implications for velocity dependent friction, *J. Geophys. Res.*, *111*, doi:10.1029/2005JB004096.

Obara, K. (2002), Nonvolcanic deep tremor associated with subduction in southwest Japan, *Science*, *296*, 1679–1681, doi:10.1126/science.1070378.

Okubo, P. G., and J. H. Dieterich (1986), State variable fault constitutive relations for dynamic slip, in *Earthquake Source Mechanics, Geophys. Monogr. Ser.*, *37*, edited by S. Das, J. Boatwright, and C. H. Scholz, pp. 25–36, AGU, Washington, D.C.

Peng, Z., J. E. Vidale, A. G. Wech, R. M. Nadeau, and K. C. Creager (2009), Remote triggering of tremor along the San Andreas Fault in central California, *J. Geophys. Res.*, *114*, B00A06, doi:10.1029/2008JB006049.

Perfettini, H., and J. Avouac (2004), Postseismic relaxation driven by brittle creep: A possible mechanism to reconcile geodetic measurements and the decay rate of aftershocks, application to the Chi-Chi earthquake, Taiwan, *J. Geophys. Res.*, *109*, B02304, doi:10.1029/2003JB002488.

Perfettini, H., J. Schmittbuhl, and A. Cochard (2003), Shear and normal load perturbations on a two-dimensional continuous fault: 2. Dynamic triggering, *J. Geophys. Res.*, *108*(B9, 2409), doi:10.1029/2002JB001805.

Rice, J. R., N. Lapusta, and K. Ranjith (2001), Rate and state dependent friction and the stability of sliding between elastically deformable solids, *J. Mech. Phys. Solids*, *49*, 1865–1898.

Rubin, A. (2011), Designer friction laws for bimodal slow slip propagation speeds, *Geochem. Geophys. Geosyst.*, *12*, Q04007, doi:10.1029/2010GC003386.

Rubinstein, J. L., M. La Rocca, J. E. Vidale, K. C. Creager, and A. G. Wech (2008), Tidal modulation of nonvolcanic tremor, *Science*, *319*, 186–189, doi:10.1126/science.1150558.

Ruina, A. L. (1983), Slip instability and state variable friction laws, *J. Geophys. Res.*, *88*, 10,359–10,370.

Savage, J. (2006), Dislocation pileup as a representation of strain accumulation on a strike-slip fault, *J. Geophys. Res.*, *111*, B04405, doi:10.1029/2005JB004021.

Scholz, C. H. (1990), *The Mechanics of Earthquakes and Faulting*, 439 pp., Cambridge Univ. Press, New York.

Scruggs, V. J. (1997), Frictional constitutive properties and related microstructures of albite, muscovite, biotite and talc, Ph. D. dissertation, Brown University, Providence, Rhode Island.

Segall, P., and A. M. Bradley (2012), Slow-slip evolves into megathrust earthquakes in 2D numerical simulations, *Geophys. Res. Lett.*, *39*, L18308, doi:10.1029/2012GL052811.

Segall, P., A. M. Rubin, A. M. Bradley, and J. R. Rice (2010), Dilatant strengthening as a mechanism for slow slip events, *J. Geophys. Res.*, *115*, B12305, doi:10.1029/2010JB007449.

Shea, W. T., and A. K. Kronenberg (1992), Rheology and deformation mechanisms of an isotropic mica schist, *J. Geophys. Res.*, *97*, 15,201–15,237.

Shelly, D. R. (2009), Possible deep fault slip preceding the 2004, Parkfield earthquake, inferred from detailed observations of tectonic tremor, *Geophys. Res. Lett.*, *36*, L17318, doi:10.1029/2009GL039589.

Shelly, D. R., and J. L. Hardebeck (2010), Precise tremor source locations and amplitude variations along the lower-crustal central San Andreas Fault, *Geophys. Res. Lett.*, *37*, L14301, doi:10.1029/2010GL043672.

Shelly, D. R., and K. M. Johnson (2011), Tremor reveals stress shadowing, deep postseismic creep, and depth-dependent slip recurrence on the lower-crustal San Andreas fault near Parkfield, *Geophys. Res. Lett.*, *381*, L13312, doi:10.1029/2011GL047863.

Shelly, D. R., G. C. Beroza, S. Ide, and S. Nakamula (2006), Low frequency earthquakes in Shikoku, Japan, and their relationship to episodic tremor and slip, *Nature*, *442*, 188–191, doi:10.1038/nature04931.

Shelly, D. R., G. C. Beroza, and S. Ide (2007a), Non-volcanic tremor and low-frequency earthquake swarms, *Nature*, *446*, 305–307, doi:10.1038/nature05666.

Shelly, D. R., G. C. Beroza, and S. Ide (2007b), Complex evolution of transient slip derived from precise tremor locations in western Shikoku, Japan, *Geochem. Geophys. Geosyst.*, *8*, Q10014, doi:10.1029/2007GC001640.

Shelly, D. R., Z. Peng, D. P. Hill, and C. Aiken (2011), Triggered creep as a possible mechanism for delayed dynamic triggering of tremor and earthquakes, *Nat. Geosci.*, *4*, 384–388, doi:10.1038/ngeo1141.

Shibazaki, B., and Y. Iio (2003), On the physical mechanism of silent slip events along the deeper part of the seismogenic zone, *Geophys. Res. Lett.*, *30*(9, 1489), doi:10.1029/2003GL017047.

Smith, E. F., and J. Gomberg (2009), A search in strainmeter data for slow slip associated with triggered and ambient tremor near Parkfield, California, *J. Geophys. Res.*, *114*, B00A14, doi:10.1029/2008JB006040.

Thomas, A. M., R. M. Nadeau, and R. Burgmann (2009), Tremor-tide correlations and near-lithostatic pore pressure on the deep San Andreas fault, *Nature*, *462*, 1048–1051, doi:10.1038/nature08654.

Thomas, A., N. M. Beeler, R. Burgmann, and D. R. Shelly (2011), The frequency dependence of friction in experiment, theory, and observations of low frequency earthquakes, Abstract S23B-2249, presented at 2011 Fall Meeting, AGU, San Francisco, Calif., 5-9 Dec.

Thomas, A. M., R. Burgmann, D. R. Shelly, N. M. Beeler, and M. L. Rudolph (2012), Tidal sensitivity of low frequency earthquakes near Parkfield, CA: Implications for fault mechanics within the brittle-ductile transition, *J. Geophys. Res.*, *117*, B05301, doi:10.1029/2011JB009036.

Townend, J., and M. D. Zoback (2000), How faulting keeps the crust strong, *Geology*, *28*, 399–402.

Vidale, J. E., D. C. Agnew, M. J. S. Johnston, and D. H. Oppenheimer (1998), Absence of earthquake correlation with Earth tides: An indication of high preseismic fault stress rate, *J. Geophys. Res.*, *103*, 24,567–24,572.

Weeks, J. D., N. M. Beeler, and T. E. Tullis (1991), Glass is like a rock, *Eos Trans. AGU*, *72*, 457–458.

Weertman, J. (1979), Inherent instability of quasi-static creep slippage on a fault, *J. Geophys. Res.*, *84*, 2146–2152.

Wilcock, W. S. (2001), Tidal triggering of microearthquakes on the Juan de Fuca Ridge, *Geophys. Res. Lett.*, *28*, 3999–4002.

Zoback, M. D., et al. (1987), New evidence on the state of stress of the San Andreas Fault system, *Science*, *238*, 1105–1111.

Erratum

In the originally published version of this article, Figure 4b is the same as Figure 4a and the embedded equations in the figure caption contain typographic errors. The figure and caption have since been corrected, and this version may be considered the authoritative version of record.